Chemical Engineering Journal 435 (2022) 134826

Contents lists available at ScienceDirect

Chemical Engineering Journal

journal homepage: www.elsevier.com/locate/cej

# Thermo-spun reaction encapsulation fabrication of environment-stable and knittable fibrous ionic conductors with large elasticity and high fatigue resistance

Qichun Feng [a], Kening Wan [c], Tianyi Zhu [a], Chao Zhang [a,*], Tianxi Liu [a,b,*]

[a] The Key Laboratory of High-Performance Fiber and Product, Ministry of Education, College of Materials Science and Engineering, Donghua University, Shanghai 201620, PR China
[b] Key Laboratory of Synthetic and Biological Colloids, Ministry of Education, School of Chemical and Material Engineering, Jiangnan University, Wuxi 214122, PR China
[c] School of Engineering and Materials Science, Queen Mary University of London, Mile End Road, London E1 4NS UK

ARTICLE INFO

*Keywords:*
Thermo-spun reaction encapsulation
Fibrous ionic conductor
Environmental stability
High fatigue resistance
Wearable strain sensor

ABSTRACT

The development of knittable fibrous ionic conductors with a wide temperature tolerance, high fatigue resistance and wearing comfort is crucial yet challenging for the emerging wearable skin sensors. Herein, a thermo-spun reaction encapsulation strategy is presented for fabricating a low-temperature tolerant and high fatigue-resistant fibrous ionic conductor. The fibrous ionic conductor demonstrates a core-sheath structure that consists of hydrogen-bonded poly(ionic liquid)-backboned ionogel (HB-PILI) and thermoplastic elastomer (TPE) as the core and sheath, respectively. Due to the combination of the ionic conductive core and highly elastic sheath, the resultant HB-PILI@TPE fiber exhibits high stretchability (>100%), wide temperature resistance (−50 ~ 50 °C), and excellent fatigue resistance (maximum stress retention of 74.3% after 5000 stretching-releasing cycles). As a result, fibrous strain sensors based on the resultant HB-PILI@TPE fiber demonstrate fast response time (less than100 ms), high-yet-linear sensitivity (gauge factor of 1.05), and excellent cyclic stability (>3000 cycles). Importantly, the fibrous sensor also shows stable responses to various strains (0 ~ 100% strain) and frequencies (0.01 ~ 0.2 Hz). Moreover, the HB-PILI@TPE fiber is capable of being easily weaved into a fabric that could maintain high mechanical elasticity in a wide temperature range. As a proof of concept, the as-assembled fibrous ionic sensor is capable of being attached to human skin and monitoring the movements of large and facet joints in real-time, showing high wearing comfort, large sensitivity and wide detecting range. Therefore, the developed fibrous ionic conductors that are fabricated by the thermo-spun reaction encapsulation method are promising for fabricating high-performance wearable skin sensors with excellent wearing comfort and high environmental tolerance.

## 1. Introduction

Fibrous strain sensors have shown the advantages of wearability, comfort and breathability, which are significantly superior to traditional strain sensors based on bulk and film materials [1,2]. Fibrous strain sensors could be easily integrated with traditional fabrics and directly weaved into a sensor fabric that could be well wrapped on curved surfaces of human body, but these are huge challenges for traditional bulk- and film-based strain sensors [3,4]. In addition, traditional bulk- and film-based strain sensors also face the problem of poor air permeability, which severely restricts their conforts as wearable strain sensors [5–7]. In contrast, fibrous strain sensors have the advantages of high air permeability, which could be worn comfortably on human skin [8,9]. Accordingly, fibrous strain sensors are expected to show spread prospects in soft robotics, health monitoring, and human–machine interfaces [10,11]. As a core component of fibrous strain sensors, the development of stretchable conductive fibers is essential [12,13]. A sufficient amount of conductive fillers needs to be introduced into non-conductive elastomers for the fabrication of stretchable conductive fibers according to the percolation theory [14,15]. However, the poor interfacial interactions between the elastomer and the conductive fillers make the stretchable electron-conducting fibers unable to balance the large

* Corresponding authors at: The Key Laboratory of High-Performance Fiber and Product, Ministry of Education, College of Materials Science and Engineering, Donghua University, Shanghai 201620, PR China.
*E-mail addresses:* czhang@dhu.edu.cn (C. Zhang), txliu@fudan.edu.cn (T. Liu).

https://doi.org/10.1016/j.cej.2022.134826
Received 25 November 2021; Received in revised form 10 January 2022; Accepted 18 January 2022
Available online 22 January 2022

deformation and high sensing performance, and thereby bring various serious problems to the resultant soft electronic skin, e.g., narrow strain range, low conductivity and poor stability [16,17]. Therefore, the development of new-type stretchable conductive fibers with high conductivity, excellent fatigue resistance and high sensitivity that could undergo large deformations and extremely low-temperature environments has important prospects while meeting a great challenge.

Ionic conductors based on directional migrations of free ions driven by voltage differences are new-type interdisciplinary materials, involving bioscience and electrochemistry [18]. The conductivity of ionic conductors is highly related to the concentration of efficient free ions in the conductive pathways, and the deformation of ionic conductors shows almost no damages to ionic conductive paths, thus the ionic conductors could ignore the limitation of the percolation theory [19,20]. In addition, ionic conductors are naturally biocompatible so they could effectively avoid serious side effects caused by the voltage drop in biological tissues [21,22]. Therefore, various ionic conductors have been used in ionic skins, ionic cables, and artificial muscles [23–25]. Typical ionic conductors are mainly composed of conductive hydrogels with water-soluble inorganic salts, which suffer from easy losses of water and narrow working temperature range [26,27]. Nevertheless, ionic conductors that are fabricated from ionogels using ionic liquids (ILs) as the solvent are capable of overcoming the weakness of easy dehydration because they could inherit the advantages of ILs [19,28]. Despite the above advantages, continuous fabrications of fibrous ionogels have not been achieved because of the poor spinnability of ionogels as well as their precursors because the time required to form ionogel networks far exceeds the time required to form fibers [15]. Wet spinning is a traditional fiber-shaping method that could efficiently produce continuous fibers on a large scale based on the mechanism of nonsolvent-induced phase separations of spinning solution in a coagulating bath [29,30]. It usually takes much time for converting the precursor solution into ionogels by thermal-initiated polymerization afterwards; however the formation of fibers from the spinning solution demands to be completed within a few seconds [31,32]. The relatively slow thermal-initiated polymerization conflicts with the rapid spinning process [33]. Coaxial fibrous structures are promising to provide a post-processing operating window for precursors that could be encapsulated in the core of coaxial fibers, and subsequent conversion from the precursors into conductive gel networks in the core is expected to be effective for fabricating conductive fibers [34]. Therefore, it remains a challenge to establish unique thermal-initiated polymerization strategies that match the spinning process to efficiently produce continuous fibrous ionogels.

Herein, we present the fabrication of a fibrous conductor that is constituted of hydrogen-bonded poly(ionic liquid) ionogel (HB-PILI) and thermoplastic elastomer (TPE) as the core and sheath, respectively. The core-sheath fiber was fabricated by a thermo-spun reaction encapsulation strategy consisting of two steps. First, a spinning solution of TPE was squeezed into the outer channel of a coaxial needle and flocculated in a coagulating bath to form a hollow TPE microtube, and simultaneously the other spinning solution of the precursor of HB-PILI was squeezed into the inner channel of the coaxial needle. Second, thermal-induced polymerization was conducted for converting the precursor within the hollow TPE microtube into HB-PILI. Among the HB-PILI@TPE fibers, the HB-PILI core inherits the advantages of ILs with high ionic conductivity, low vapor pressure and high thermal stability, whereas the TPE sheath endows the fiber with outstanding elasticity and high fatigue resistance. Benefiting from the strong interfacial interactions between the in-situ formed HB-PILI and TPE, the resultant HB-PILI@TPE fibers demonstrate low hysteresis, wide detecting range, linear-yet-high sensitivity as a stretchable fibrous conductor in a resistance-type strain sensor. Moreover, the knittable HB-PILI@TPE fibers could be woven into a fabric, which still maintains high mechanical elasticity in a wide temperature range. As a proof of concept, the fibrous ionic sensor based on the resultant HB-PILI@TPE fibers is capable of monitoring human joint movements in real-time when being attached to human skin. The thermo-spun reaction encapsulation strategy therefore opens an avenue to fabricate stretchable and knittable fibrous ionic conductors with wide-temperature tolerance and high fatigue resistance for high-sensitivity, wide-response-range and durable wearable skin sensors.

## 2. Materials and methods

### 2.1. Fabrication of HB-PILI@TPE fibers

The HB-PILI@TPE fibers were fabricated by a thermo-spun reaction encapsulation method. The sheath spinning solution was prepared by dissolving 10 g of TPE into 20 g of $CH_2Cl_2$ under stirring. The core spinning solution was prepared as follows: 1 mL of 1-vinyl-3-ethylimidazolium dicyanamide ([Veim][DCA], monomer I), 400 mg of acrylamide (AM, monomer II), 8 mg of *N*,*N*′-methylene bisacrylamide (MBA, crosslinker) and 30 mg of ammonium persulfate (APS, initiator) were dissolved in 3 mL of 1-ethyl-3-methylimidazolium dicyanamide ([Emim][DCA], ILs as the solvent) at room temperature. All the spinning solution was degassed for 10 min before wet-spun. A coaxial needle constituted of a 21-gauge (21G) inner channel and 15-gauge (15G) outer channel was used for the subsequent thermo-spun reaction encapsulation. The sheath spinning solution was squeezed into an ethanol coagulation bath through the outer channel of the coaxial needle at a speed of 400 μL $min^{-1}$, and a hollow TPE microtube was quickly formed. Meanwhile, the core spinning solution was injected into the inner channel at a speed of 200 μL $min^{-1}$, thus forming an intermediate core-sheath fiber abbreviated as Pre@TPE. The final HB-PILI@TPE fiber was then obtained by thermal treatment of Pre@TPE at 60 °C for 6 h for achieving in-situ polymerization of the core precursor. The HB-$PILI_{19G}$@$TPE_{15G}$, HB-$PILI_{23G}$@$TPE_{15G}$, HB-$PILI_{21G}$@$TPE_{13G}$ and HB-$PILI_{21G}$@$TPE_{17G}$ represent the HB-PILI@TPE samples obtained by tailoring the inner/outer channel diameters of the coaxial needle. Hollow TPE fiber was fabricated by extracting the HB-PILI core from the as-spun HB-PILI@TPE fiber, and the extracted fiber from the core was denoted as HB-PILI fiber. A comparison sample of PILI without the formation of dense hydrogen-bonded interaction was prepared by in-situ polymerization of 1 mL of [Veim][DCA] in 3 mL of [Emim][DCA]. Another comparison sample of PAM hydrogel (PAMH) was prepared by in-situ polymerization of 400 mg of AM and 8 mg of MBA in 3 mL of water at 60 °C for 6 h by using 30 mg of APS as an initiator.

### 2.2. Measurements of fibrous ionic sensors

TPE sheath could melt and form a viscous fluid above ~ 70 °C, and copper wires could be wrapped by the viscous TPE fluid under stress. Fibrous ionic sensor of HB-PILI@TPE was obtained by hot-pressing. In particular, a HB-PILI@TPE fiber with two copper wires pre-placed inside at both ends was placed in a hot-pressing mold, and then the pressure was set at 1 MPa while the time for hot-pressing was set at 30 s. The as-obtained fibrous ionic sensor was settled in a motorized actuating system, consisting of a tensile testing machine (UTM2000, SANS) and a source meter (2612B, Keithley). The resultant fibrous ionic sensor was attached to human skin to monitor the joint movements of a volunteer.

## 3. Results and discussion

Fig. 1a is a schematic diagram of the HB-PILI@TPE fiber that is fabricated by the thermo-spun reaction encapsulation strategy. The sheath spinning solution of TPE solution was squeezed through the outer channel of the coaxial needle, and the core spinning solution containing the precursor was meanwhile injected through the inner channel of the coaxial needle, thus obtaining the Pre@TPE fiber. The Pre@TPE fiber was subsequently thermally treated for converting the core precursor into the HB-PILI through heat-triggered free-radical copolymerization of AM and [Veim][DCA] in the solvent of [Emim][DCA] (Fig. 1b). During

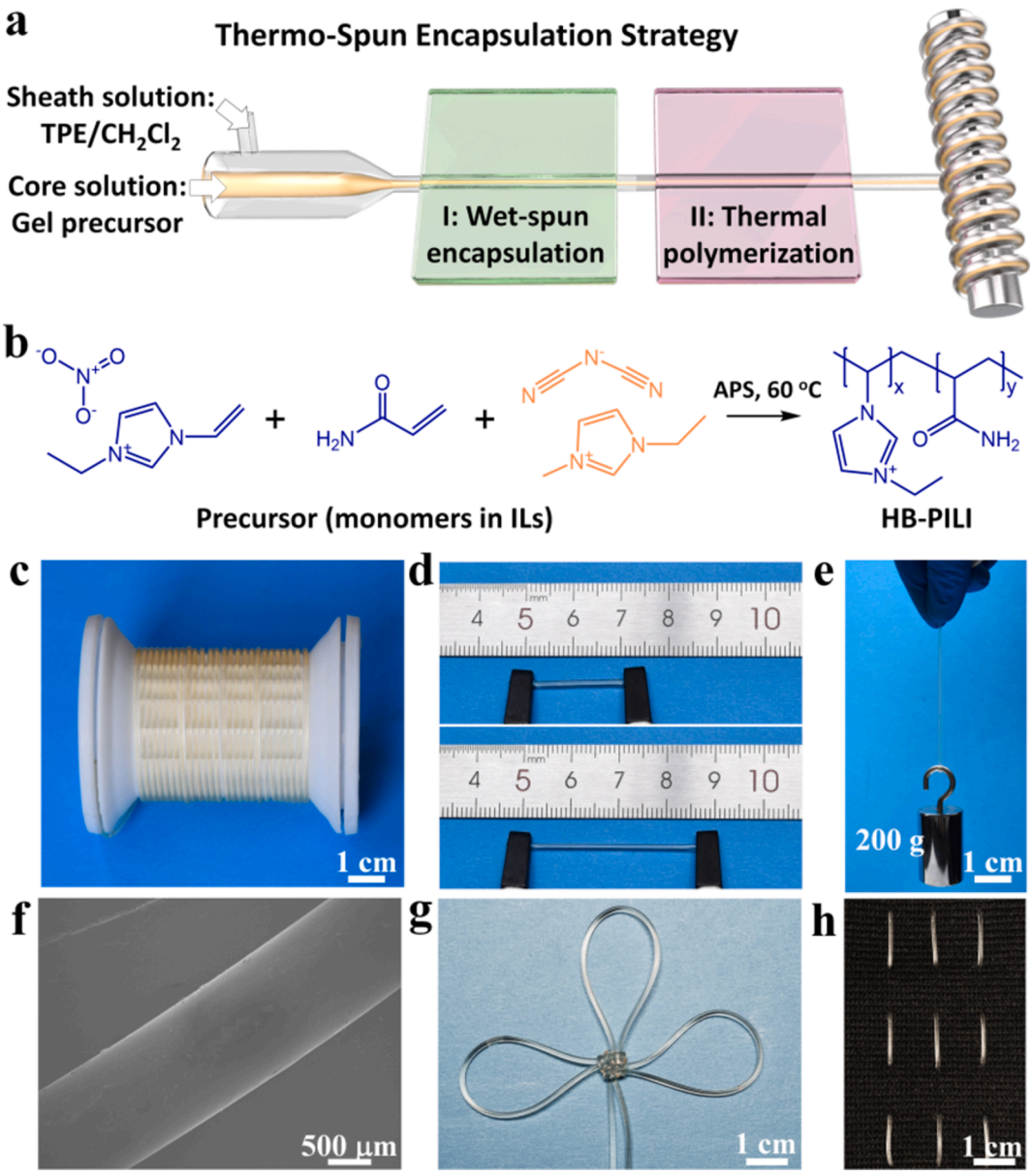


**Fig. 1.** (a) Schematic of the fabrication of the HB-PILI@TPE fiber by the thermo-spun reaction encapsulation strategy. (b) Heat-triggered polymerization of the HB-PILI. Photographs showing the HB-PILI@TPE fibers (c) collected on a spindle, (d) stretched at a 100% strain, and (e) holding a 200 g weight. (f) Surface SEM image of the HB-PILI@TPE fiber. (g) Photograph showing the HB-PILI@TPE fiber woven into a knot. (h) Photograph showing the blended fabrics woven with the HB-PILI@TPE and conventional fibers.

the thermal treatment, the small amount of $CH_2Cl_2$ remaining in the as-spun sheath layer was evaporated, yielding the TPE sheath with excellent elastic property. The continuous length of the resultant HB-PILI@TPE fiber was easily >5 m, indicating that the thermo-spun reaction encapsulation strategy has the potential to produce core-sheath ionic conductive fibers in a large scale (Fig. 1c). The HB-PILI@TPE fiber is capable of being stretched to a 100% strain (Fig. 1d) and holding a 200 g weight (Fig. 1e). No cracks were observed after the HB-PILI@TPE fiber withstanding multi-time force deformations, showing that the fiber has an excellent mechanical elasticity. After 5000 stretching/releasing cycles, the surface morphologies of HB-PILI@TPE fiber were still smooth (Fig. 1f), suggesting that the HB-PILI@TPE fiber has excellent structural stability. The HB-PILI@TPE fiber is easily tied into knots, showing its high flexibility (Fig. 1g). Furthermore, the weaving of HB-PILI@TPE fiber with conventional fibers into fabrics makes the HB-PILI@TPE fiber possible to be integrated into wearable fabrics for practical applications (Fig. 1h).

The ionic liquid of [Emim][DCA] as the solvent of the core precursor has a very low vapor pressure. The TPE sheath could further block any leakages of [Emim][DCA]. For surface SEM observations, HB-PILI@TPE fibers were directly sputter-coated with a thin gold layer. For facture-surface SEM observations, HB-PILI@TPE fibers were submerged into liquid nitrogen and fractured, and then a thin gold layer was sputtered on the facture surface before SEM observation. The core diameters of the core-sheath fibers can be controlled by tailoring the sizes of the inner channels of coaxial needles. The core diameters of core-sheath fibers of the $HB\text{-}PILI_{19G}@TPE_{15G}$, $HB\text{-}PILI_{21G}@TPE_{15G}$ and $HB\text{-}PILI_{23G}@TPE_{15G}$ decrease to 1050, 1000 and 950 μm (Fig. 2a-2c), when the sizes of inner channels are controlled as 19G, 21G and 23G, respectively. When the outer channels are kept at 15G, the diameters of the whole fiber are stable at ~ 1200 μm. It is worth noting that the diameters of the TPE sheath can not be controlled by tailoring the diameters of outer channels. The sheath diameters of $HB\text{-}PILI_{21G}@TPE_{13G}$, $HB\text{-}PILI_{21G}@TPE_{15G}$ and $HB\text{-}PILI_{21G}@TPE_{17G}$ are retained at 1200 ~ 1250 μm (Fig. 2d-2f),

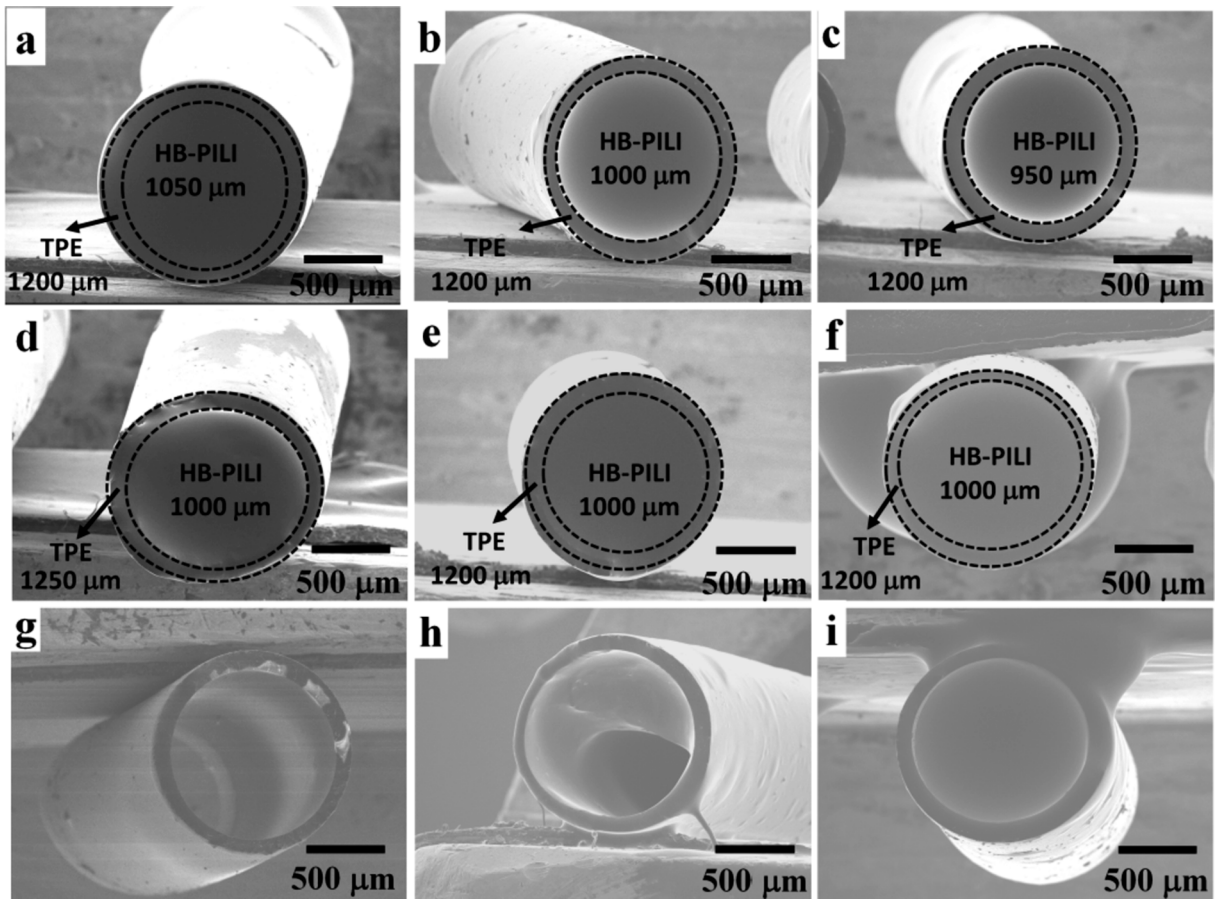


**Fig. 2.** Fracture-surface SEM images of (a) HB-PILI$_{19G}$@TPE$_{15G}$, (b) HB-PILI$_{21G}$@TPE$_{15G}$, (c) HB-PILI$_{23G}$@TPE$_{15G}$, (d) HB-PILI$_{21G}$@TPE$_{13G}$, (e) HB-PILI$_{21G}$@TPE$_{15G}$ and (f) HB-PILI$_{21G}$@TPE$_{17G}$. Fracture-surface SEM images of Pre@TPE after thermal polymerization for (g) 2 h, (h) 4 h and (i) 6 h, respectively, followed with ethanol washing.

when the inner channels are kept at 21G, and the outer channels are controlled as 13G, 15G and 17G, respectively. This phenomenon is attributed to that when the $CH_2Cl_2$ in the sheath spinning solution is solvent exchanged by ethanol to form hollow TPE microfiber, and the hollow TPE microfiber would continue to collapse until the core precursor solution is wholely encapsulated. Compared with gases, the intermolecular free volume between liquid molecules is substantially reduced, and therefore the volume of liquids is hard to be compressed [35]. Since the construction of core-sheath fibers requires the formation of a hollow microtube first, the inner channel of coaxial needles needs to be fixed in the middle within the outer channel. After being squeezed out by a syringe pump, the incompressible spinning solution in the core could be immediately wrapped by the sheath spinning solution [16]. Therefore, the diameters of the resultant HB-PILI@TPE fibers depend on the diameters of the incompressible spinning solution in the core. The effect of the time for heat-triggered polymerization on the diameter of the HB-PILI core was also investigated (Fig. 2g-2i). After in-situ polymerization for 2 h, the HB-PILI core is still in its liquid state. With the increased polymerization time, the HB-PILI core gradually changes from a quasi-gel state (Fig. 2h) to a gel state (Fig. 2i).

Fig. 3a is a photograph of HB-PILI retained in an inverted vial, indicating that the gel network of HB-PILI was formed during the thermal treatment [36]. Thermogravimetric analysis (TGA) manifests that the weight of HB-PILI decreases slightly at the beginning, due to a small amount of water being absorbed within the HB-PILI (Fig. 3b). When the temperature climbs to 192 °C, an obvious weight decrease is observed due to the decomposition of the HB-PILI network [37]. The results show that the gel network of HB-PILI is stable below 192 °C, indicating the HB-PILI has the potential to work up to 192 °C.

Fourier transform infrared spectra (FT-IR) is an important characterization to analyze the evolutions of functional groups during polymerization and their interactions [38–40]. To investigate the interface between the PAMH and PILI backbones, neat PAMH and PILI were respectively synthesized. The PAMH was characterized by FT-IR spectroscopy after freeze-drying. The FT-IR peaks of $–NH_2$ (3200 ~ 3300 $cm^{-1}$) and -C = O (1635 $cm^{-1}$) belong to the PAMH [41]. The N-heterocycle groups at 2000 ~ 2300 $cm^{-1}$ belong to the HB-PILI (Fig. 3c). These peaks in HB-PILI are superimposed by the PAMH and PILI, and these peaks slightly shift, indicating that the [Veim][DCA] and [Emim][DCA] are both introduced into the gel network of PAMH during thermal polymerization. It should be pointed out that the slight shifts ascribing to the $–NH_2$ in PAMH (1670, 3400 $cm^{-1}$) and HB-PILI (1650, 3300 $cm^{-1}$) are attributed to the formation of hydrogen bonds between the $–NH_2$ and [Emim][DCA] [42–44]. In-situ FT-IR spectra at various temperatures directly reflect the influences of the temperatures on the molecular structures. Fig. 3d is in-situ FT-IR spectra of HB-PILI at various temperatures. It should be pointed out that the heating rate of the in-situ FT-IR measurements was set at 2 °C per minute, and the spectra were collected at 1 Hz with a resolution of 2.0 $cm^{-1}$. The influences of the temperatures on the molecular structures of HB-PILI could be accurately recorded by the in-situ FT-IR spectra. With the increased temperatures, no significant shifts are observed. Taking the [DCA] (at ~ 2125 $cm^{-1}$) as an example, the intensity and shift of peaks ascribing to the [DCA] are consistent at various temperatures. The results indicate that the chemical structures of HB-PILI are stable within the temperature range of 0 ~ 100 °C. The influences of the PAMH backbone on the mechanical properties of HB-PILI were studied (Fig. S1). The elongation at break of HB-PILI increases 2.2 times compared with that of PILI, and the fracture

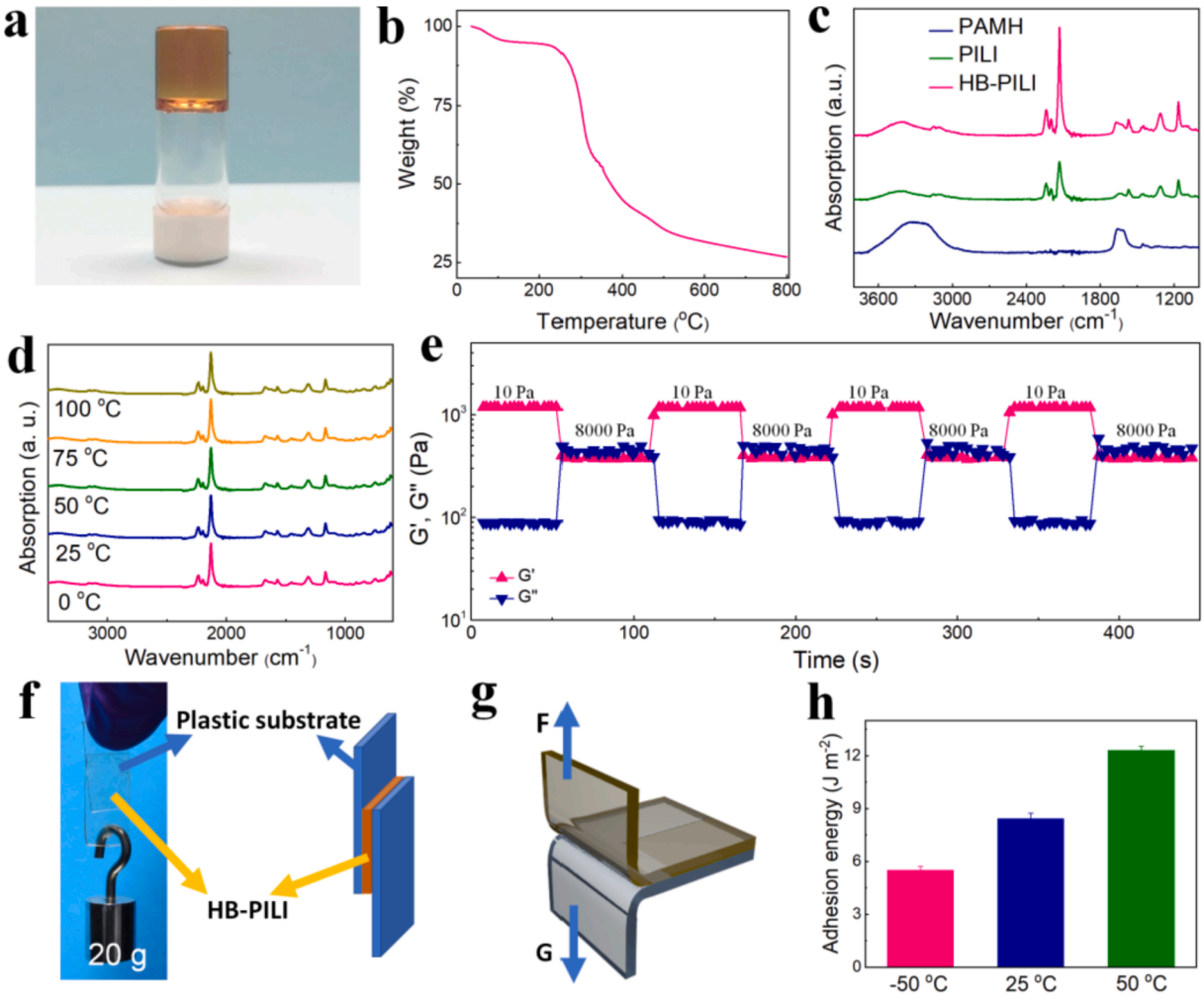


**Fig. 3.** (a) Photograph showing an inverted vial of the HB-PILI. (b) TGA curve of the HB-PILI in a nitrogen atmosphere. (c) FT-IR spectra of PAMH, PILI and HB-PILI. (d) FT-IR spectra of HB-PILI at various temperatures. (e) Continuous step-stress measurements of HB-PILI at 10 and 8000 Pa. (f) Photograph showing the HB-PILI film adhering to two TPE substrates. (g) Schematic characterization methods for the adhesion performance. (h) Adhesion performance of HB-PILI at various temperatures.

mechanical strength increases 1.55 times. The intermolecular interactions could improve the compactness of the gel networks and endow the gels with high mechanical properties [38]. Hydrogen bonds between the $–NH_2$ and –COOH groups could be easily formed in the system [45,46]. The excellent mechanical properties of HB-PILI are attributed to the presence of hydrogen bonds introduced by PAMH networks. Therefore, the introduction of PAMH backbones effectively improves the mechanical properties of neat PILI.

More than that, the influence of PILI on the anti-freezing performance of HB-PILI was also studied by differential scanning calorimetry (DSC) (Fig. S2). A sharp peak near 0 °C is observed on the DSC curve for PAMH, indicating that the PAMH has a relatively high freezing point due to the presence of water. For the PILI and HB-PILI, no DSC peaks are observed in the temperature range of −75 ~ 5 °C. The results show that the PILI backbone can effectively improve the anti-freezing performance of HB-PILI. The strain sweep measurements of HB-PILI between 1 and 500 Pa were measured (Fig. S3a), showing that the values of storage modulus (G′) are much higher than that of loss modulus (G″). The linear response of G′ and G″ is observed in the range of angular frequencies of 1 ~ 100 rad $s^{-1}$ (Fig. S3b). The results suggest that the elastic characteristics of the HB-PILI are consistent with other ionogels in the literature, and the gel network is successfully formed. Continuous step-stress measurements were used to simulate external forces on the HB-PILI. In particular, small stress has less interference to gel networks, which could be used to measure the gel networks under a static environment. Large stress could break the gel networks, which is typically used to measure the gel networks under external forces. Small stress (10 Pa) was applied to the HB-PILI, the G′ values are much higher than that of G″, indicating that the HB-PILI networks are stable at small stress (Fig. 3e). When the applied stress shifts to 8000 Pa, the values of G′ decrease rapidly, which are slightly inferior to the G″ values. The results show that the elastic network structures of HB-PILI are destroyed by the applied large stress. The small stress (10 Pa) is re-applied to the HB-PILI, and the values of G′ and G″ return to their original states within a few seconds, showing the gel network of HB-PILI has a high-efficient self-healing ability.

In-situ attenuated total reflectance FT-IR spectra (ATR FT-IR) during rheological measurements are widely used to evaluate the structural evolutions of soft materials under external forces [47]. Here, in-situ ATR FT-IR measurements during the rheological measurements were used to investigate the HB-PILI networks under the applied stress (Fig. S4a). The FT-IR peaks of [DCA] (~2125 $cm^{-1}$) belong to the HB-PILI at the small stress, and a significant shift of the peak (2130 $cm^{-1}$) is observed at the large stress. The results manifest that the [DCA] is released from the PAMH gel network, showing the HB-PILI network was partially destroyed. The [DCA] peak shifts back to its original state at the small applied stress, indicating that most of the [DCA] were re-absorbed into the PAMH network (Fig. S4b). The excellent self-healing ability of HB-PILI gives the HB-PILI@TPE fiber the potential to withstand repeated large strains. Fig. S5 is the temperature-responsive sweep measurements of HB-PILI. Within the temperature range of 0 ~ 100 °C, the G′ and G″

values of HB-PILI are almost the same, indicating that the gel networks of HB-PILI are stable in a wide temperature range .

The interfacial interaction between the HB-PILI core and TPE sheath was further investigated. Fig. 3f is an optical photograph of HB-PILI adhering to two separate TPE films. The sandwiched film is capable of withstanding a weight of 20 g, showing that the HB-PILI has an excellent adhesive ability on TPE. For further investigating the adhesion performance of HB-PILI, the HB-PILI and TPE films are fixed at the bottom and top (Fig. 3g), respectively, by using a tensile testing machine clamping the HB-PILI film. The adhesion energy was calculated from Equation (1):

$$\Gamma = \frac{(F - G)^{*}L}{S} \tag{1}$$

where Γis the adhesion energy, F is the stretching force, G is the gravity of gel, L is the tearing distance, and S is the adhesion area. The adhesion force is positively proportional to the temperature (Fig. 3h), which is attributed to the temperature-responsive properties of intermolecular interactions between the TPE backbone and *N*-heterocycle in HB-PILI (i.e., π- π, π -n interactions) [48,49]. Before investigating strain sensing performances of bulk ionogels, hydrophobic elastomer films were used to encapsulate ionogels [45]. The adhesion between ionogels and elastomer films is positive for the response time [50]. Therefore, the high adhesion performance is beneficial for HB-PILI@TPE fiber to quickly respond to external stimuli.

Fig. 4 shows the mechanical properties of HB-PILI@TPE fibers. The HB-PILI@TPE and hollow TPE fibers were stretched for 5000 cycles at a 100% strain, respectively. The maximum stress loss of HB-PILI@TPE fibers in the first 10 cycles is 8.7 kPa, which is attributed to a slight mechanical mismatch between the HB-PILI core and TPE sheath in HB-PILI@TPE fibers (Fig. 4a) [51]. After 100 cycles of repeated stretching, the inevitable fatigue loss occurs on the TPE sheath, and the maximum stress loss of HB-PILI@TPE fiber reaches 11.7 kPa. The results are attributed to the internal stress release of HB-PILI@TPE fiber during tensile. In the following cycles, the maximum stress loss of HB-PILI@TPE fiber gradually decreased. After 3000 cycles, the maximum stress loss only expands to 17.7 kPa, and the final maximum stress loss is only 18 kPa, yielding the maximum stress retention of 74.3%. Compared to that of hollow TPE fiber (Fig. 4b), the HB-PILI@TPE fiber presents excellent mechanical properties after 5000 cycles. The results are attributed to the HB-PILI core being able to avoid the stress concentration [52]. The maximum stresses of the HB-PILI@TPE and hollow TPE fibers were summarized in Fig. 4c. In the primary 3000 cycles, the maximum stress loss of hollow TPE fiber decreases stepwise, indicating that the stress concentration destroys the microstructure of hollow TPE fiber. With these microstructures being destroyed, the maximum stress of hollow TPE fiber shows a stable decline after 3000 cycles. Fig. 4d is the loading–unloading curves of HB-PILI@TPE fiber at various frequencies. Each time-stress curve of the HB-PILI@TPE fiber is almost symmetrical, which further confirms the excellent mechanical properties of HB-PILI@TPE fiber [53]. The mechanical properties of fibers are also able to be evaluated by calculating the energy loss during the loading/unloading process. Fig. 4e shows the energy loss of HB-PILI@TPE fiber at the first loading/unloading cycle. The work during loading (*U*) is 0.25 mJ, and the work (energy dissipation (Δ*U*)) remains at 0.047 mJ after completely unloading.

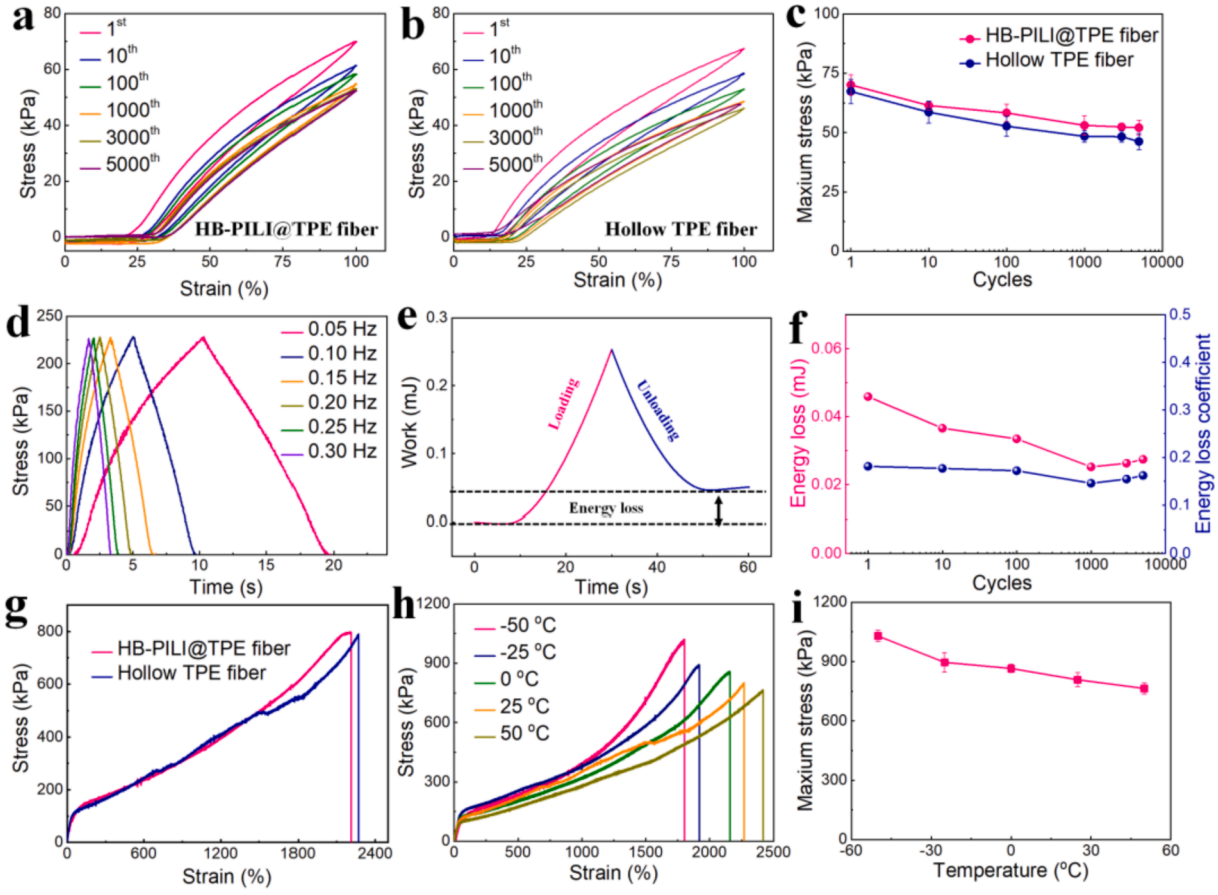


**Fig. 4.** Mechanical properties of the HB-PILI@TPE fiber. Cyclic loading/unloading tests of (a) HB-PILI@TPE and (b) hollow TPE fibers. (c) Maximum stress of HB-PILI@TPE and hollow TPE fibers. (d) Time-dependent stress response of HB-PILI@TPE fiber. (e) Tensile work and energy loss of HB-PILI@TPE fiber at the first cycle. (f) Cycle-dependent energy loss and energy loss coefficient of HB-PILI@TPE fiber. (g) Strain-stress curves of HB-PILI@TPE and hollow TPE fibers. (h) Strain-stress curves of HB-PILI@TPE fiber at various temperatures. (i) Maximum stress of HB-PILI@TPE fiber at various temperatures.

$$\eta = \frac{\Delta U}{U} \quad (2)$$

An almost constant energy loss (0.037 ~ 0.027 mJ) of HB-PILI@TPE fiber is observed based on the loss coefficient (η) of Equation (2). Its energy loss coefficient is calculated at 0.16 ~ 0.18 except for the first cycle (Fig. 4f). The highly efficient energy dissipation of HB-PILI@TPE fiber in the first cycle is attributed to plastic deformation [54,55]. Similar to that of the HB-PILI@TPE fiber, the hollow TPE fiber also tends to mechanical performance failure, but the failure amplitude of hollow TPE fiber is higher than that of HB-PILI@TPE fiber (Fig. S6). More than that, the fracture mechanical strength of the HB-PILI@TPE fiber is only slightly higher than that of hollow TPE (Fig. 4g), indicating that the HB-PILI would not decrease the mechanical properties of TPE sheath. Fig. S7 shows that the HB-PILI has a relatively low modulus and high fatigue resistance. The elongation at break of the HB-PILI@TPE fiber is similar to that of hollow TPE fiber, showing that the HB-PILI core would not influence the tensile properties of the TPE sheath. The influences of temperature on the mechanical properties of HB-PILI@TPE fiber were also investigated (Fig. 4h). The fracture mechanical strength of the HB-PILI@TPE fiber decreases with the increasing temperatures (Fig. 4i), while the elongation at break is proportional to temperature. The results are attributed to the temperature affecting the crystalline structures of the TPE sheath. In particular, the glassy transition temperatures of TPE sheath are at −60 and 70 °C, respectively. Although the TPE sheath could not be transformed into the glassy state at −50 °C, the low temperature would still decrease the movements of TPE chains, and the free volume of chains are also decreased at the low temperature. It should be pointed out the HB-PILI core is retained at its gel state between −50 and 50 °C, and the large environmental temperature changes do not affect the mechanical properties of the HB-PILI core as well as TPE sheath.

Fig. 5 shows the endurance of HB-PILI@TPE fibers at extreme temperatures. The HB-PILI@TPE fibers were placed at various temperatures (−50 ~ 50 °C) for 7 weeks, and there are almost no changes in the weight. The results present that the HB-PILI@TPE fiber has excellent stability at extreme temperatures (Fig. 5a). Since the TPE sheath has a small polarity, water molecules could not infiltrate into the TPE [56]. The elastomer materials with a small polarity are widely used in the packaging of strain sensors [57]. Therefore, the results of weight changes at various temperatures are ascribed to the high hydrophobicity of the TPE sheath that could prevent water molecules from infiltrating into the core of HB-PILI@TPE fibers. The conductivities of HB-PILI@TPE fiber at various temperatures are significantly different, which are owing to the temperatures positively correlated with the rates of ion migration (Fig. 5b). However, the conductivity of HB-PILI@TPE fiber is constant at a certain temperature. The results indicate that the HB-PILI@TPE fiber has excellent conductivity stability at extreme temperatures, which is

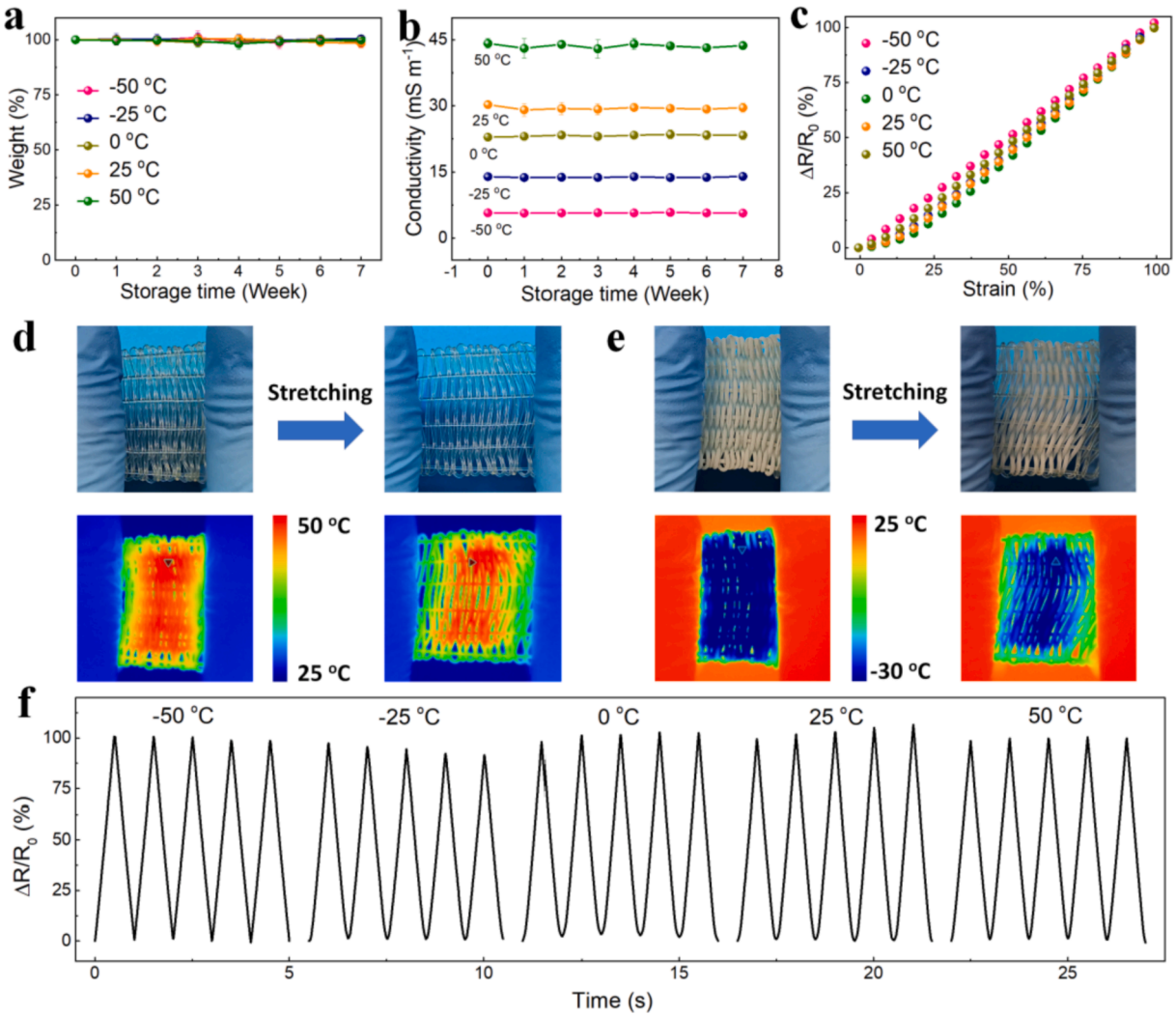


**Fig. 5.** Extreme temperature tolerance of the HB-PILI@TPE fiber. Changes of (a) weight and (b) conductivity at various temperatures. (c) GF values at various temperatures. Photographs showing the stretching process of the HB-PILI@TPE-based fabric at (d) high and (e) low temperatures. (f) Relative resistance changes of HB-PILI@TPE fibrous ionic sensor at various temperatures.

attributed to the formation of the gel state of the HB-PILI core at extreme temperatures. The gauge factor (GF) values of the fibrous sensor based on HB-PILI@TPE fiber are similar at various temperatures, and the GF values are calculated as 1.03 ($R^2 = 0.99$), 1.01 ($R^2 = 0.99$), 0.99 ($R^2 = 0.99$), 1.02 ($R^2 = 0.99$), 0.99 ($R^2 = 0.99$), respectively (Fig. 5c). The results show that the fibrous ionic sensor is capable of working in a wide temperature range. The fabric woven by HB-PILI@TPE fiber can be stretched at 50 °C (Fig. 5d) and −30 °C (Fig. 5e). The results show that the HB-PILI@TPE fiber has excellent elastic properties under extreme temperatures, which gives the fiber potentials to be a wearable skin sensor for hot desert and extremely cold Antarctic environments. It should be pointed out that the white color on the surface of HB-PILI@TPE fibers is attributed to the condensation of water from the air on the fiber surface at a low temperature (Fig. 5e). Fig. S2 shows that the freezing point of the HB-PILI core is lower than −75 °C, and the glass transition temperatures of the TPE sheath are −60 °C and 70 °C, respectively. Therefore, the lowest working temperature of HB-PILI@TPE fiber and its fabric is −60 °C. The HB-PILI@TPE fibrous ionic sensor was placed at various temperatures to monitor cyclic 100% strains (Fig. 5f). The similar working curves under different temperatures further confirm that the fibrous ionic sensor can work stably at various temperatures.

Fig. 6 shows the sensing performance of the HB-PILI@TPE fibrous ionic sensor. Under different strains, stepped working curves are presented and consistent with the applied strains (Fig. 6a). The heights of two neighboring curves are in multiple relationships, indicating that the HB-PILI@TPE fibrous ionic sensor is strain-dependent. With the increasing frequencies, the working curves are gradually dense (Fig. 6b), suggesting that the HB-PILI@TPE fibrous ionic sensor is frequency-dependent. The hysteresis determines the continuous working performance of the strain sensor, which is calculated by the area enclosed by the working curves [46,58]. Fig. 6c shows the area enclosed by the working curve of the HB-PILI@TPE fibrous ionic sensor is very small, indicating that the HB-PILI@TPE fibrous ionic sensor has an extremely low hesitation. The results are attributed to the high adhesion between HB-PILI core and TPE sheath, which realizes the synchronized movements of sheath and core for coaxial fibers. The response time determines the ability of strain sensors to quickly respond to external stimuli. Fig. 6d shows that the stretching response time of the HB-PILI@TPE fibrous ionic sensor is less than 120 ms, and the releasing response time is also less than 100 ms. The extremely fast response time is attributed to the high tensile recovery properties of HB-PILI and TPE. Moreover, the resistances of the HB-PILI@TPE fibrous ionic sensor keep almost the same before and after stretching, indicating that the conductive paths of HB-PILI are not be damaged by the stretching. Fig. 6e exhibits the durability of the HB-PILI@TPE fibrous ionic sensor. The insets in Fig. 6e are the working curves of the HB-PILI@TPE fibrous ionic sensor at different stages (initial, intermediate and final stages). The HB-PILI@TPE fibrous ionic sensor can output repeatable working curves without obvious decays after stretching for > 3000 cycles (12000 s) under a frequency of 0.25 Hz, indicating that the HB-PILI@TPE fibrous ionic sensor has a long-term working life. Therefore, the intriguing properties with high anti-freezing performance, large deformation, high GF values, long-term working life, and high conductivity of HB-PILI@TPE fiber are suitable for applications in wearable strain sensors (Fig. S8).

Fig. 7 shows the wearable performance of the fibrous ionic sensor of HB-PILI@TPE. The insets in Fig. 7a-7f manifest that the HB-PILI@TPE fibrous ionic sensor is directly worn on human skin for detecting joint movements. The wearing and testing of the HB-PILI@TPE fibrous ionic sensor indicate its high wearable comfort. Fig. 7a and 7b demonstrate that the HB-PILI@TPE fibrous ionic sensor can monitor the movements of the wrist and knee, respectively. The results show that large joint movements can be monitored by the HB-PILI@TPE fibrous ionic sensor. The human finger movements were monitored by the fibrous sensor (Fig. 7c). More than that, the GF values of the HB-PILI@TPE fibrous ionic sensors used for monitoring different angles of finger bendings are calculated to be 0.32 (30°), 0.61 (60°), and 0.78 (90°), respectively, showing that the fibrous sensor has a high sensitivity (Fig. 7d). Similarly, the HB-PILI@TPE fibrous ionic sensor can monitor the movements of the elbow joint at various angles (Fig. 7e, 7f). Movie S1 shows that the HB-PILI@TPE sensor could be worn on a human knee, and the marching movements could be accurately captured in real-time by the fibrous sensor. Therebefore, the HB-PILI@TPE fibrous ionic sensor has high wearable comfort and can delicately monitor the movements of human large and facet joints.

## 4. Conclusion

In summary, a fibrous ionic conductor with a unique core-sheath

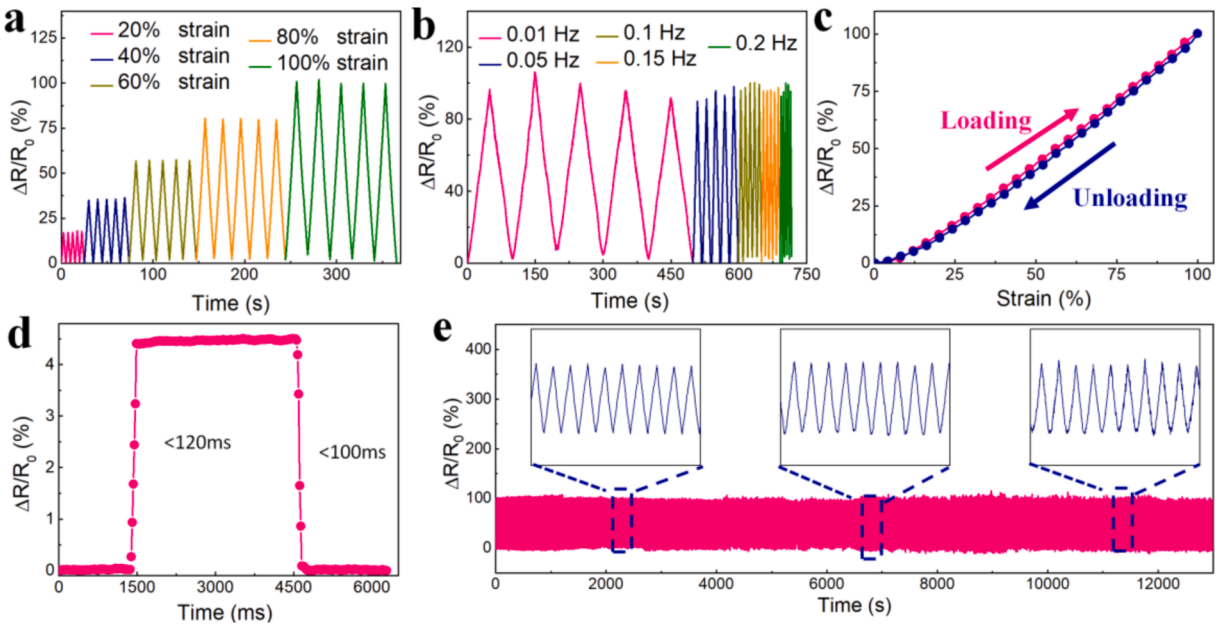


**Fig. 6.** Strain sensing performance of the HB-PILI@TPE fibrous strain sensor. Relative resistance changes at various (a) strains and (b) frequencies. (c) Hysteresis performance, (d) response time, and (e) cycling stability.

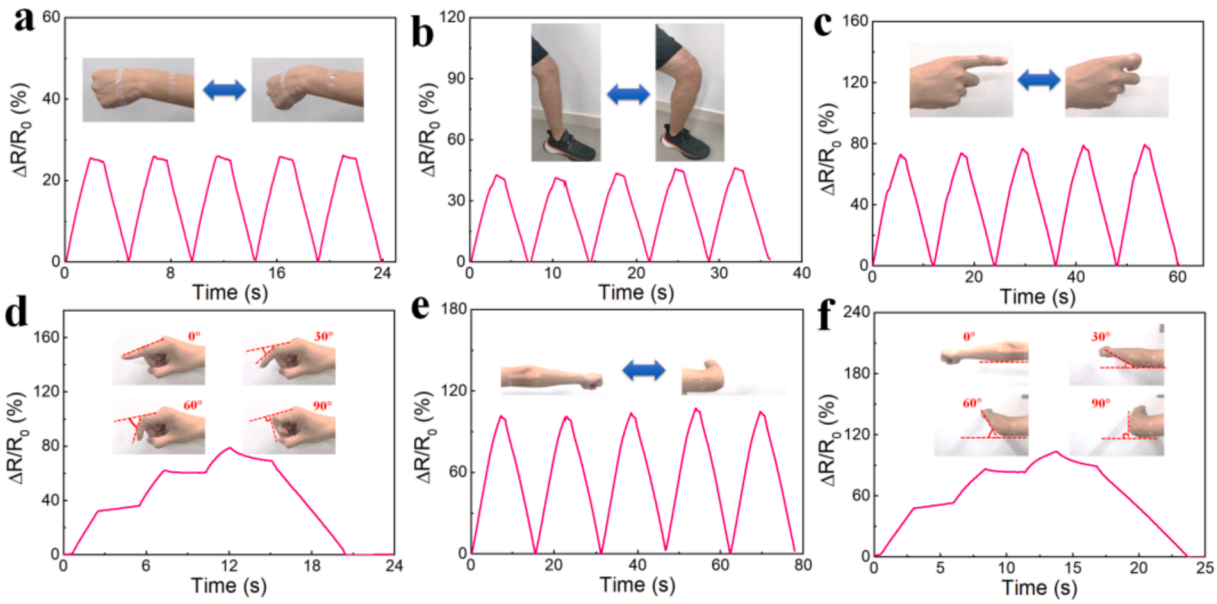


**Fig. 7.** Wearable sensing performance of the HB-PILI@TPE fibrous strain sensor. Relative resistance changes of the sensor monitoring bendings of (a) wrist, (b) knee, (c) finger, (d) finger with various bending angles, (e) elbow, and (f) elbow with various bending angles.

structure is fabricated by a thermo-spun reaction encapsulation strategy. The precursor of HB-PILI was injected into the hollow TPE microtube by a coaxial wet-spinning, and the [Veim][DCA] and AM were thermo-polymerized into an ionogel. [Emim][DCA] was closely embedded into the ionogel network through hydrogen bonding. The coaxial structure of HB-PILI@TPE fiber can be controlled by tailoring the channel diameter of coaxial needles. The HB-PILI@TPE fiber demonstrates superior structural stability with maximum stress retention of > 74% after being stretched for 5000 cycles. The excellent conductivity of HB-PILI endows the core-sheath fiber with high conductivity of 44 mS $m^{-1}$. The excellent adhesion between the HB-PILI core and the TPE sheath gives the HB-PILI@TPE fiber an extremely low hysteresis. The anti-freezing performance of the HB-PILI core ensures the core-sheath fiber with a stable conductivity at various temperatures (−50 ~ 50 °C). The high hydrophobicity of TPE sheath endows high environmental stability with a weight change of less than 1% after being placed for 7 weeks. The fabric woven with the HB-PILI@TPE fiber shows high mechanical elasticity in a wide temperature range. The working curves of the HB-PILI@TPE fibrous ionic sensor are similar at various environmental temperatures. The HB-PILI@TPE fibrous ionic sensor can work stably under variable deformations (0 ~ 100% strain) for>12000 s and under various strain frequencies (0.01 ~ 0.20 Hz). Moreover, the wearable sensing performance of the HB-PILI@TPE fibrous ionic sensor has also been conceptually verified. The HB-PILI@TPE fibrous ionic sensor can be directly attached to human skin, and large and facet deformations of human joints are capable of being delicately captured by the ionic sensor. This thermo-spun reaction encapsulation strategy thus opens a new avenue to fabricate fibrous ionic conductors with large elasticity and high fatigue resistance.

## Declaration of Competing Interest

The authors declare that they have no known competing financial interests or personal relationships that could have appeared to influence the work reported in this paper.

## Acknowledgements

This work is supported by the Fundamental Research Funds for the Central Universities (2232020G-02), the National Natural Science of China (52122303, 21875033).

## Appendix A. Supplementary data

Supplementary data to this article can be found online at https://doi.org/10.1016/j.cej.2022.134826.

## References

[1] Y. Zhang, Display textiles: Illuminating the way we live, Sci. China Chem. 64 (2021) 1115–1116.
[2] Y. Zheng, Y. Li, Y. Zhou, K. Dai, G. Zheng, B. Zhang, C. Liu, C. Shen, High-performance wearable strain sensor based on graphene/cotton fabric with high durability and low detection limit, ACS Appl. Mater. Interfaces 12 (1) (2020) 1474–1485.
[3] H. Wang, Y. Zhang, X. Liang, Y. Zhang, Smart fibers and textiles for personal health management, ACS Nano 15 (8) (2021) 12497–12508.
[4] K. Zhou, K. Dai, C. Liu, C. Shen, Flexible conductive polymer composites for smart wearable strain sensors, SmartMat 1 (2020) 1010.
[5] C. Wang, K. Xia, H. Wang, X. Liang, Z. Yin, Y. Zhang, Advanced carbon for flexible and wearable electronics, Adv. Mater. 31 (2019) 1801072.
[6] C. You, W. Qin, Z. Yan, Z. Ren, J. Huang, J. Ii, W. Chang, W. He, K. Wen, S. Yin, X. Zhou, Z. Liu, Highly improved water tolerance of hydrogel fibers with a carbon nanotube sheath for rotational, contractile and elongational actuation, J. Mater. Chem. A 9 (16) (2021) 10240–10250.
[7] X. Yue, Y. Jia, X. Wang, K. Zhou, W. Zhai, G. Zheng, K. Dai, L. Mi, C. Liu, C. Shen, Highly stretchable and durable fiber-shaped strain sensor with porous core-sheath structure for human motion monitoring, Compos. Sci. Technol. 189 (2020), 108038.
[8] W. Zeng, L. Shu, Q. Li, S. Chen, F. Wang, X.-M. Tao, Fiber-based wearable electronics: A review of materials, fabrication, devices, and applications, Adv. Mater. 26 (2014) 5310–5336.
[9] J. Shi, S. Liu, L. Zhang, B. Yang, L. Shu, Y. Yang, M. Ren, Y. Wang, J. Chen, W. Chen, Y. Chai, X. Tao, Smart textile-integrated microelectronic systems for wearable applications, Adv. Mater. 32 (2020) 1901958.
[10] S. Liu, K. Ma, B. Yang, H. Li, X. Tao, Textile electronics for VR/AR applications, Adv. Funct. Mater. 31 (39) (2021), 2007254.
[11] Q. Gao, M. Wang, X. Kang, C. Zhu, M. Ge, Continuous wet-spinning of flexible and water-stable conductive pedot: PSS/PVA composite fibers for wearable sensors, Compos. Commun. 17 (2020) 134–140.
[12] Q. Ma, B. Hao, P. Ma, Modulating the sensitivity of a flexible sensor using conductive glass fibre with a controlled structure profile, Compos. Commun. 20 (2020), 100367.
[13] Q. Gao, P. Wang, M. Wang, Y. Wang, J. Zhu, Metal salt modified PEDOT: PSS fibers with enhanced elongation and electroconductivity for wearable e-textiles, Compos. Commun. 25 (2021), 100700.
[14] F. Guan, Y. Xie, H. Wu, Y. Meng, Y. Shi, M. Gao, Z. Zhang, S. Chen, Y. Chen, H. Wang, Q. Pei, Silver nanowire–bacterial cellulose composite fiber-based sensor for highly sensitive detection of pressure and proximity, ACS Nano 14 (11) (2020) 15428–15439.

[15] J. Song, S. Chen, L. Sun, Y. Guo, L. Zhang, S. Wang, H. Xuan, Q. Guan, Z. You, Mechanically and electronically robust transparent organohydrogel fibers, Adv. Mater. 32 (2020) 1906994.
[16] X. Tang, D. Cheng, J. Ran, D. Li, C. He, S. Bi, G. Cai, X. Wang, Recent advances on the fabrication methods of nanocomposite yarn-based strain sensor, Nanotechnol. Rev. 10 (1) (2021) 221–236.
[17] Y. Jiang, Z. Liu, C. Wang, X. Chen, Heterogeneous strain distribution of elastomer substrates to enhance the sensitivity of stretchable strain sensors, Acc. Chem. Res. 52 (1) (2019) 82–90.
[18] D. Gao, P. Lee, Lee Pooi, Rectifying ionic current with ionoelastomers, Science 367 (6479) (2020) 735–736.
[19] M. Yao, B. Wu, X. Feng, S. Sun, P. Wu, A highly robust ionotronic fiber with unprecedented mechanomodulation of ionic conduction, Adv. Mater. 33 (2021) 2103755.
[20] Z. Lei, W. Zhu, X. Zhang, X. Wang, P. Wu, Bio-inspired ionic skin for theranostics, Adv. Funct. Mater. 31 (2021) 2008020.
[21] K. Zhao, K. Zhang, R. Li, P. Sang, H. Hu, M. He, A very mechanically strong and stretchable liquid-free double-network ionic conductor, J. Mater. Chem. A 9 (41) (2021) 23714–23721.
[22] Y. Gao, J. Guo, J. Chen, G. Yang, L. Shi, S. Lu, H. Wu, H. Mao, X. Da, G. Gao, S. Ding, Highly conductive organic-ionogels with excellent hydrophobicity and flame resistance, Chem. Eng. J. 427 (2022), 131057.
[23] X. Shi, P. Wu, A smart patch with on-demand detachable adhesion for bioelectronics, Small 17 (2021) 2101220.
[24] C. Wan, P. Cai, X. Guo, M. Wang, N. Matsuhisa, L. Yang, Z. Lv, Y. Luo, X. Loh, X. Chen, An artificial sensory neuron with visual-haptic fusion, Nat. Commun. 11 (2020) 4602.
[25] M. Zou, S. Li, X. Hu, X. Leng, R. Wang, X. Zhou, Z. Liu, Progresses in tensile, torsional, and multifunctional soft actuators, Adv. Funct. Mater. 31 (2021) 2007437.
[26] Y. Zhao, Z. Li, S. Song, K. Yang, H. Liu, Z. Yang, J. Wang, B. Yang, Q. Lin, Skin-inspired antibacterial conductive hydrogels for epidermal sensors and diabetic foot wound dressings, Adv. Funct. Mater. 29 (2019) 1901474.
[27] X. Sui, H. Guo, C. Cai, Q. Li, C. Wen, X. Zhang, X. Wang, J. Yang, L. Zhang, Ionic conductive hydrogels with long-lasting antifreezing, water retention and self-regeneration abilities, Chem. Eng. J. 419 (2021), 129478.
[28] T. Li, X. Zhang, S. Lacey, R. Mi, X. Zhao, F. Jiang, J. Song, Z. Liu, G. Chen, J. Dai, Y. Yao, S. Das, R. Yang, R. Briber, L. Hu, Cellulose ionic conductors with high differential thermal voltage for low-grade heat harvesting, Nat. Mater. 18 (6) (2019) 608–613.
[29] J. Zeng, W. Ma, Q. Wang, S. Yu, M.T. Innocent, H. Xiang, M. Zhu, Strong, high stretchable and ultrasensitive SEBS/CNTs hybrid fiber for high-performance strain sensor, Compos. Commun. 25 (2021), 100735.
[30] Q. Ma, B. Yang, H. Li, J. Guo, S. Zhao, G. Wu, Preparation and properties of photochromic regenerated silk fibroin/tungsten trioxide nanoparticles hybrid fibers, Compos. Commun. 27 (2021), 100810.
[31] L. Xu, Z. Huang, Z. Deng, Z. Du, T. Sun, Z. Guo, K. Yue, A transparent, highly stretchable, solvent-resistant, recyclable multifunctional ionogel with underwater self-healing and adhesion for reliable strain sensors, Adv. Mater. 33 (2021) 2105306.
[32] N. Jiang, X. Chang, D. Hu, L. Chen, Y. Wang, J. Chen, Y. Zhu, Flexible, transparent, and antibacterial ionogels toward highly sensitive strain and temperature sensors, Chem. Eng. J. 424 (2021), 130418.
[33] R. Shi, Y. Tian, L. Wang, Bioinspired fibers with controlled wettability: From spinning to application, ACS Nano 15 (2021) 7907–7930.
[34] J. Ren, X. Sun, P. Chen, Y. Wang, H. Peng, Research progress of fiber-shaped electrochemical energy storage devices, Chin. Sci. Bull. 65 (28-29) (2020) 3150–3159.
[35] M. Gado, S. Ookawara, S. Nada, I. El-Sharkawy, Hybrid sorption-vapor compression cooling systems: A comprehensive overview, Renew. Sust. Energ. Rev. 143 (2021) 110912, https://doi.org/10.1016/j.rser.2021.110912.
[36] B. Zhang, X. Zhang, K. Wan, J. Zhu, J. Xu, C. Zhang, T. Liu, Dense hydrogen-bonding network boosts ionic conductive hydrogels with extremely high toughness, rapid self-recovery, and autonomous adhesion for human-motion detection, Research 2021 (2021) 9761625.
[37] K. Huang, C. Hsiao, Y. Nien, J. Lin, Synthesis, characterization, and application of PVP/PAM copolymer, J. Appl. Polym. Sci. 99 (5) (2006) 2454–2459.
[38] Y. Wang, M. Tebyetekerwa, Y. Liu, M. Wang, J. Zhu, J. Xu, C. Zhang, T. Liu, Extremely stretchable and healable ionic conductive hydrogels fabricated by surface competitive coordination for human-motion detection, Chem. Eng. J. 420 (2021), 127637.
[39] Q. Feng, K. Wan, C. Zhang, T. Liu, Cryo-spun encapsulation of polyaniline-based conducting hydrogels with high sensitivity, wide-range linearity, and environmental stability for fibrous strain sensors, J. Polym. Sci. (2021), https://doi.org/10.1002/pol.20210766.
[40] L. Li, J. Meng, M. Zhang, T. Liu, C. Zhang, Recent advances in conductive polymer hydrogel composites and nanocomposites for flexible electrochemical supercapacitors, Chem. Commun. 58 (2) (2021) 185–207.
[41] J. Tan, J. Zhang, C. Li, Y. Luo, S. Ye, Ultrafast energy relaxation dynamics of amide i vibrations coupled with protein-bound water molecules, Nat. Commun. 10 (2019) 1010.
[42] S. Batten, K. Murray, Structure and magnetism of coordination polymers containing dicyanamide and tricyanomethanide, Coord. Chem. Rev. 246 (1–2) (2003) 103–130.
[43] J. Yu, Y. Dai, Q. He, D. Zhao, Z. Shao, M. Ni, A mini-review of noble-metal-free electrocatalysts for overall water splitting in non-alkaline electrolytes, Mater. Reports: Energy 1 (2021), 100024.
[44] L. Zhang, Q. Shao, J. Zhang, An overview of non-noble metal electrocatalysts and their associated air cathodes for mg-air batteries, Mater. Reports: Energy 1 (2021), 100002.
[45] A. Wang, Y. Wang, B. Zhang, K. Wan, J. Zhu, J. Xu, C. Zhang, T. Liu, Hydrogen-bonded network enables semi-interpenetrating ionic conductive hydrogels with high stretchability and excellent fatigue resistance for capacitive/resistive bimodal sensors, Chem. Eng. J. 411 (2021), 128506.
[46] P. Shi, Y. Wang, W. Tjiu, C. Zhang, T. Liu, Highly stretchable, fast self-healing, and waterproof fluorinated copolymer ionogels with selectively enriched ionic liquids for human-motion detection, ACS Appl. Mater. Interfaces 13 (41) (2021) 49358–49368.
[47] B. Chiou, S. Khan, Real-time FTIR and in situ rheological studies on the UV curing kinetics of thiol-ene polymers, Macromolecules 30 (23) (1997) 7322–7328.
[48] F. Liu, J. Wang, Q. Pan, An all-in-one self-healable capacitor with superior performance, J. Mater. Chem. A 6 (6) (2018) 2500–2506.
[49] L. Bai, Y. Han, C. Sun, X. An, C. Wei, W. Liu, M. Xu, L. Sun, N. Sun, M. Yu, H. Zhang, Q. Wei, C. Xu, Y. Yang, T. Qin, L. Xie, J. Lin, W. Huang, Unveiling the effects of interchain hydrogen bonds on solution gelation and mechanical properties of diarylfluorene-based semiconductor polymers, Research 2020 (2020) 3405826.
[50] P. Lu, L. Wang, P. Zhu, J. Huang, Y. Wang, N. Bai, Y. Wang, G. Li, J. Yang, K. Xie, J. Zhang, B. Yu, Y. Dai, C. Guo, Iontronic pressure sensor with high sensitivity and linear response over a wide pressure range based on soft micropillared electrodes, Sci. Bull. 66 (11) (2021) 1091–1100.
[51] Y. Tang, Y. Xu, J. Yang, Y. Song, F. Yin, W. Yuan, Stretchable and wearable conductometric VOC sensors based on microstructured MXene/polyurethane core-sheath fibers, Sens. Actuators, B 346 (2021), 130500.
[52] Y. Xu, Q. Feng, C. Zhang, T. Liu, Wet-spinning of ionic liquid@elastomer coaxial fibers with high stretchability and wide temperature resistance for strain sensors, Compos. Commun. 25 (2021), 100693.
[53] F. Zhang, Y. Feng, M. Qin, L. Gao, Z. Li, F. Zhao, Z. Zhang, F. Lv, W. Feng, Stress controllability in thermal and electrical conductivity of 3D elastic graphene-crosslinked carbon nanotube sponge/polyimide nanocomposite, Adv. Funct. Mater. 29 (2019) 1901383.
[54] Z. Liu, K. Wan, T. Zhu, J. Zhu, J. Xu, C. Zhang, T. Liu, Superelastic, fatigue-resistant, and flame-retardant spongy conductor for human motion detection against a harsh high-temperature condition, ACS Appl. Mater. Interfaces 13 (6) (2021) 7580–7591.
[55] L. Li, Y. Zhang, H. Lu, Y. Wang, J. Xu, J. Zhu, C. Zhang, T. Liu, Cryopolymerization enables anisotropic polyaniline hybrid hydrogels with superelasticity and highly deformation-tolerant electrochemical energy storage, Nat. Commun. 11 (2020) 62.
[56] G. Baeza, Recent advances on the structure–properties relationship of multiblock copolymers, J. Polym. Sci. 59 (21) (2021) 2405–2433.
[57] T. Chen, Y. Xie, Z. Wang, J. Lou, D. Liu, R. Xu, Z. Cui, S. Li, M. Panahi-Sarmad, X. Xiao, Recent advances of flexible strain sensors based on conductive fillers and thermoplastic polyurethane matrixes, ACS Appl. Polym. Mater. 3 (11) (2021) 5317–5338.
[58] Y. Wang, Y. Liu, R. Plamthottam, M. Tebyetekerwa, J. Xu, J. Zhu, C. Zhang, T. Liu, Highly stretchable and reconfigurable ionogels with unprecedented thermoplasticity and ultrafast self-healability enabled by gradient-responsive networks, Macromolecules 54 (8) (2021) 3832–3844.